Reference and Target Region Modeling of [^{11}C]-(*R*)-PK11195 Brain Studies

Federico E. Turkheimer[1–3], Paul Edison[1,3], Nicola Pavese[3], Federico Roncaroli[4], Alexander N. Anderson[1], Alexander Hammers[1,5], Alexander Gerhard[3,6], Rainer Hinz[2], Yan F. Tai[1,3], and David J. Brooks[1–3]

[1]Division of Neuroscience, Department of Clinical Neuroscience, Imperial College London, London, United Kingdom; [2]Hammersmith Imanet, Hammersmith Hospital, London, United Kingdom; [3]PET Neurology Group, MRC CSC, Hammersmith Hospital, London, United Kingdom; [4]Division of Neuroscience, Department of Neuropathology, Imperial College London, London, United Kingdom; [5]PET Epilepsy Group, Hammersmith Hospital, London, United Kingdom; and [6]Department of Psychiatry, University of Mainz, Germany

PET with [^{11}C]-(*R*)-PK11195 is currently the modality of choice for the in vivo imaging of microglial activation in the human brain. In this work we devised a supervised clustering procedure and a new quantification methodology capable of producing binding potential (BP) estimates quantitatively comparable with those derived from plasma input with robust quantitative implementation at the pixel level. **Methods:** The new methodology uses predefined kinetic classes to extract a gray matter reference tissue without specific tracer binding and devoid of spurious signals (in particular, blood pool and muscle). Kinetic classes were derived from an historical database of 12 healthy control subjects and from 3 patients with Huntington's disease. BP estimates were obtained using rank-shaping exponential spectral analysis (RS-ESA) (both plasma and reference input) and the simplified reference tissue model (SRTM). Comparison between plasma-derived BPs and those produced with the new reference methodology was performed using 6 additional healthy control subjects. Reliability of the new methodology was performed on 4 test–retest studies of patients with Alzheimer's disease. **Results:** The new algorithm selected reference voxels in gray matter tissue avoiding regions with specific binding located, in particular, in the venous and arterial circulation. Using the new reference, BP values obtained using a plasma input and a reference input were in excellent agreement and highly correlated ($r = 0.811$, $P < 10^{-5}$) when calculated with RS-ESA and less so ($r = 0.507$, $P < 0.005$) when SRTM was used. In the production of parametric maps, SRTM was used with the new reference extraction, resulting in test–retest variability (10.6%; mean ICC = 0.878) that was superior to that obtained using the previous unsupervised clustering approach (mean ICC = 0.596). **Conclusion:** Reference region modeling combined with supervised reference tissue extraction produces a robust and reproducible quantitative assessment of [^{11}C]-(*R*)-PK11195 studies in the human brain.

Key Words: PET; PK11195; microglia; supervised clustering

J Nucl Med 2007; 48:158–167

A selective ligand for the peripheral benzodiazepine receptor (PBBS) is PK11195. The PBBS is a nuclear-encoded mitochondrial protein that is abundant in peripheral organs—particularly in adrenal glands, kidney, as well as hematogenous cells—but is present in the normal central nervous system only at low levels (*1*). The function of the PBBS is still in need of full elucidation but the receptor is known to play an important role in steroid synthesis and in the regulation of immunologic responses by mononuclear phagocytes (*2*).

In diseases of the central nervous system, a higher density of PBBS has been observed in macrophages and activated microglia, the intrinsic immune defense of the brain (*3*). Significant microglial activation occurs after mild-to-severe neuronal damage resulting from traumatic, inflammatory, degenerative, and neoplastic disease (*3*). Microglia, therefore, act as sensors for pathologic events, including subtle ones without any obvious structural damage (*4*), and are activated not only in the surroundings of focal lesions but also in the distant, anterograde and retrograde projection areas of the lesioned neural pathway and even in structurally normal transsynaptic areas (*5,6*).

The high selectivity for the PBBS has made PK11195 the ligand of choice for the in vivo imaging of activated microglia with PET. PET imaging with the molecular marker [^{11}C]-(*R*)-PK11195 (*7*) now provides an indicator of active disease in the brain with wide applicability (*3*).

MATERIALS AND METHODS

Methodologic Aspects of PK11195 PET Studies

Quantification of [^{11}C]-(*R*)-PK11195 PET studies has so far been approached either by normalization of the uptake to a reference region or by application of the simplified reference tissue model (SRTM) (*8*). Full kinetic characterization of [^{11}C]-(*R*)-PK11195 with measurement of the arterial input function has been reported only recently with the application of the appropriate 2-tissue compartments, 4-rate-constants model (Fig. 1) (*9*).

Further work has shown that blood input modeling provides binding potentials (BP = k3/k4) that correlate significantly with those estimated with the simplified reference region model (*10*).

Received May 22, 2006; revision accepted Sep. 25, 2006.

For correspondence or reprints contact: Federico E. Turkheimer, PhD, Division of Neuroscience and Mental Health, Department of Clinical Neuroscience, DuCane Rd., London W12 0NN, U.K.

E-mail: federico.turkheimer@imperial.ac.uk

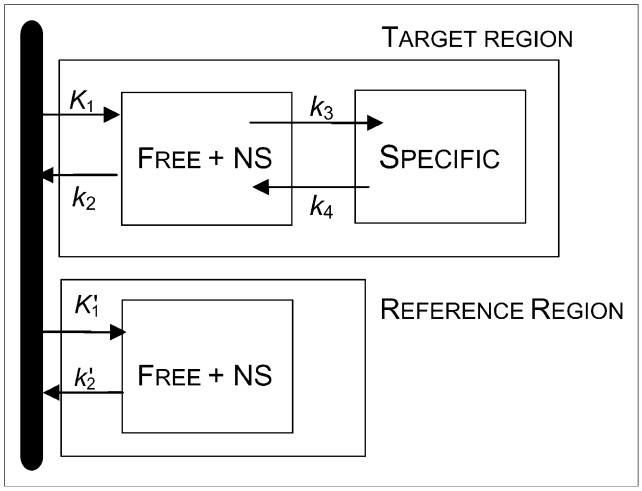

FIGURE 1. Compartmental model for [^{11}C]-(*R*)-PK11195 assumes a target region with a specific bound fraction and a compartment for a free fraction plus possibly a nonspecific bound fraction (NS) that equilibrates fast with the unbound fraction. The (ideal) reference region should be devoid of PBBSs and, therefore, be fitted best with a 1-tissue compartment model. *K*1 and *k*2 represent first-order rate constants for transport of ligand from plasma to tissue and vice versa (*K*1′ and *k*2′ for reference region); *k*3 and *k*4 represent rate constants between the free and specifically bound compartments in tissue.

However, the same studies highlighted large differences between the BP estimates obtained from blood input modeling (BP ~ 1.6 in cortical gray matter in controls) and those calculated with a tissue reference (BP ~ 0.07–0.46) (*9*). This difference could have resulted from the presence of significant nonspecific binding in brain tissue (*7*). However, BP values obtained from plasma input and corrected for nonspecific binding calculated from the reference region were still higher than SRTM BP values indicating, among several possible data and model deficiencies, the presence of specific binding in the reference used (*10*).

The use of a tissue input function may provide practical advantages, but the selection of a reference region devoid of PBBS is a challenging task. Microglia are distributed ubiquitously throughout the brain and their activation may occur along projections into healthy-appearing tissue (*3*). Furthermore, activation of microglia is associated with aging even in the normal brain (*11*).

The use of postmortem data for the selection of appropriate reference regions devoid of active microglia may be valuable in specific diseases and can increase [^{11}C]-(*R*)-PK11195 sensitivity even with small sample sizes (*12*). When an informed choice is not possible, an alternative approach is the use of cluster analysis that segments voxels into classes on the basis of their time courses and selects as reference the class of voxels that exhibits the kinetic behavior closest to that of gray matter in healthy controls (*13*).

Improved Reference Region Extraction: Scope and Rationale

Here we present an improved clustering algorithm for the automatic extraction of a reference tissue region for the quantification of [^{11}C]-(*R*)-PK11195 PET studies. Improvement was sought on 3 different grounds. The first aim was to increase the reliability of current clustering methodology that is based on unsupervised tissue classification. An unsupervised clustering algorithm defines tissue classes in a data-dependent manner according to a very generic model (e.g., a mixture of gaussian distributions) that may not accurately describe the underlying physiology and, therefore, introduce instability or inaccuracies in the grouping.

Second, we considered an algorithmic design that aimed at the extraction of a proper reference region, whereby "proper" meant that its use as input function would produce BP values comparable with those obtained with a blood input function.

Third, we considered further methodologic developments in the BP calculations that could accommodate the improved modeling of the reference region and produce robust and reproducible BP estimates.

Supervised Clustering of [^{11}C]-(*R*)-PK11195 Studies

In the normal brain, immunocytochemical staining suggests the presence of PBBS in muscle cells of small- and medium-sized intraparenchymal arteries and in the bigger leptomeningeal arteries; in perivascular macrophages, lymphocytes, and neutrophils; in the choroid plexus; and in the ependyma (Fig. 2). Other regions with a rich density of receptors include the meninges, olfactory bulbs, and the pituitary gland (*3*). Given the limited spatial resolution of PET images, specific binding in these areas is a likely source of diffuse low-level [^{11}C]-(*R*)-PK11195−specific signal that may easily affect the reference region even in healthy control subjects.

This observation commanded the use of a supervised clustering approach to extract a gray matter reference region filtered from unwanted contributions from the described sources. At the same

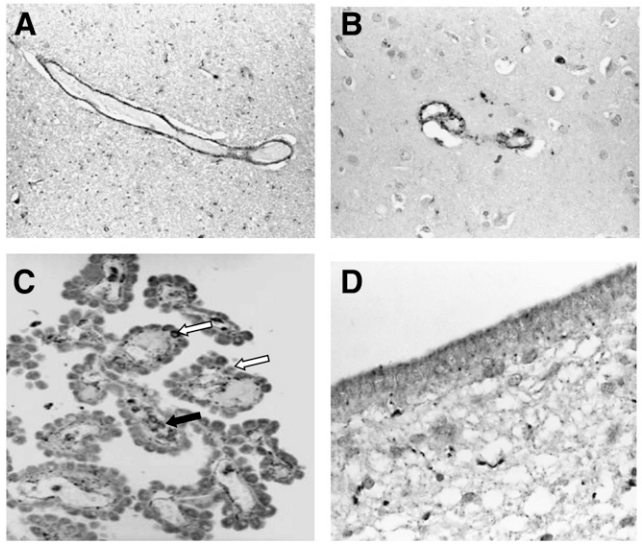

FIGURE 2. Immunostaining of PBBS in normal brain (monoclonal, clone 8D7 [kindly supplied by Dr. Pier Casellas, Department of Immunology–Oncology, Sanofi Synthelabo, Montpellier, France], dilution 1:200). Expression of PBBS is seen in smooth muscle cells of tunica media of medium-sized artery in cerebellar white matter (A) and of small cortical artery of frontal cortex (B). (C) PBBS expression is seen in some cuboidal cells (white arrows) of choroid plexus and in some macrophages in underlying fibrovascular core (black arrow). (D) Ependymal cells show expression of PBBS, which is mainly localized in apical cytoplasm.

time, the use of a supervised approach was expected to increase the robustness of the region extraction as demonstrated in previous applications (*14*).

Scanning Protocol

All [^{11}C]-(*R*)-PK11195 studies were performed on an ECAT EXACT 3D (CTI/Siemens) PET camera with 23.4-cm axial field of view, 95 transaxial planes (*15*). To reduce the effect of activity outside the direct field of view in brain scans, the tomograph was equipped with annular side shielding. A transmission scan was acquired before every emission using a single rotating photon point source of 150 MBq of ^{137}Cs for subsequent attenuation correction and scatter correction. The spatial resolution of the images reconstructed using the reprojection algorithm with the ramp and Colsher filters set to Nyquist frequency is close to isotropic: 5.1-mm (full width at half maximum [FWHM]) transaxially and 5.9-mm FWHM axially (*15*).

Subjects consisted of 12 healthy control subjects injected with 185 MBq without arterial blood sampling, 6 healthy controls injected with 296 MBq for whom an arterial input function was available, 3 patients with Huntington's disease (HD) (296 MBq injected) (*16*), and 4 patients with Alzheimer's disease (AD) scanned twice (296 MBq injected for each scan) with a maximum time interval of 6 wk (no blood sampling available for the patient group). [^{11}C]-(*R*)-PK11195 was provided by Hammersmith Imanet plc.

Thirty seconds after the start of the emission scan, [^{11}C]-(*R*)-PK11195 was infused intravenously over 10 s in 5 mL physiologic saline. Emission data were then acquired over 60 min in list mode and rebinned as 18 time frames (30-s background frame, 1 × 15-s frame, 1 × 5-s frame, 1 × 10-s frame, 1 × 30-s frame, 4 × 60-s frames, 7 × 300-s frames, and 2 × 600-s frames). Subjects were placed in the scanner oriented parallel to the orbitomeatal line, and head positioning was monitored throughout the scan. Volumetric T1-weighted MR images were obtained on a 1.0-T Picker HPQ scanner (Picker International) at the Robert Steiner MR Unit, Hammersmith Hospital, London.

Ethical approval was granted by the Hammersmith Hospitals Trust Ethics Committee, and permission to administer radioisotopes was granted by the Administration of Radioactive Substances Advisory Committee of the Department of Health, U.K. Informed written consent was obtained from all patients and healthy volunteers.

Blood Sampling Protocol

Blood input data were available for 6 control subjects. For these subjects, arterial whole-blood activity was monitored continuously for the first 15 min of the scan with a bismuth germanate coincidence detector at a flow rate of 5 mL/min (*17*). Eight discrete arterial blood samples were taken at 5, 10, 15, 20, 30, 40, 50, and 60 min into heparinized syringes. The activity concentrations of the whole blood and plasma were measured.

Five plasma samples per scan (at 5, 10, 20, 40, and 60 min) were analyzed for metabolites using a semiautomated system with online solid-phase extraction followed by reverse-phase chromatography with online radioactivity and ultraviolet detectors and integration system (*18*).

For the generation of the plasma input functions, the time course of the plasma-to-blood ratio obtained from the 8 discrete arterial samples was fitted to a model. On average, the ratio started at ~1.4 and steadily decreased to ~1.3 at 60 min, and the function of choice was the straight line:

$$\mathrm{POB}(t) = p_0 + p_1 \cdot t, \qquad \text{Eq. 1}$$

where POB(t) is the plasma over blood ratio, p_0 and p_1 are the coefficients of the linear model, and t is time.

Next, the measurement of the arterial whole-blood activity obtained from the continuous detector system was multiplied with that ratio to obtain a total plasma activity curve for the first 15 min of the scan. This curve was then combined with the discrete plasma activity concentration measurements at 20, 30, 40, 50, and 60 min to form an input function describing the total plasma activity concentration for the entire scan.

Finally, the input function of the activity concentration due to unmetabolized [^{11}C]-(*R*)-PK11195 in plasma was created by multiplying the total plasma activity input function with the function obtained from the fit of the model for the parent fraction in plasma with the 5 measurements of the parent compound during the scan. The mathematic model for the description of the amount of parent compound in plasma was the following equation:

$$\mathrm{PARENT}\ (t) = (1 - q_2) \cdot \exp(-q_1 \cdot t) + q_2 - q_3 \cdot t, \qquad \text{Eq. 2}$$

with $q_i > 0$.

This function describes an exponential approach to a falling straight line, beginning at 1 for $t = 0$.

Data Processing

The clustering code described in the following sections was implemented using Matlab (The Mathworks Inc.) on a SUN Ultra10 workstation (Sun Microsystems, Inc.). Statistical parametric mapping SPM2 (Functional Imaging Laboratory, Wellcome Department of Imaging Neuroscience, University College London, London) was used for PET/PET and PET/MRI coregistration, normalization to the MNI/ICBM152 space (MNI is Montreal Neurological Institute. ICBM is International Consortium for Brain Mapping), as well as MRI segmentation. An in-house package for tracer kinetic modeling written in Matlab was used for the kinetic analysis of the time–activity curves and blood data processing. Parametric maps of BP values using SRTM were calculated using the software package RPM written in Matlab (*19*). Statistical analysis of region-of-interest (ROI) values was performed in SPSS version 13 (SPSS Inc.).

Algorithm Implementation

The supervised clustering algorithm developed for the analysis of dynamic [^{11}C]-(*R*)-PK11195 data consisted of 3 elements:

- An input normalization procedure to scale each volume of the dynamic sequence.
- A set of predefined kinetic classes.
- A regression procedure to calculate the contribution of each kinetic class to each pixel's kinetic.

Dynamic studies were normalized by subtracting from each frame its mean and dividing it by its SD to create a unit input (*14*). This created for each pixel i the normalized kinetic $P_i^n(t)$ for the N pixels in the PET volume. Six kinetic classes were predefined: nonspecific gray matter, nonspecific white matter, pathologic PBBS binding, blood pool, skull, and muscle. If $K_j^n(t)$ is the

normalized kinetic for class j, where j = 1, . . ., 6, the supervised clustering algorithm modeled the kinetic of each pixel as a weighted linear combination of the class kinetics as:

$$P_i^n(t) = \sum_{j=1}^{6} w_{ij} K_j^n(t), \qquad \text{Eq. 3}$$

with $w_{ij} \geq 0$.

Because the kinetic classes $K_j^n(t)$ are not orthogonal, the weights w_{ij} were constrained to be positive by solving Equation 3 with the nonnegative least-squares algorithm (*20*).

Solution of Equation 3 created a volumetric map of weights w_{ij} for each class j. The reference region time–activity curve $R_1(t)$ (where j = 1 refers to the gray matter class) was finally calculated as a weighted average of the (unnormalized) pixel time–activity curves as:

$$R_1(t) = \sum_{i=1}^{N} w_{i1} P_i(t) / \sum_{i=1}^{N} w_{i1}. \qquad \text{Eq. 4}$$

Definition of Classes 1 and 2: Normal Gray and White Matter

Gray and white matter kinetics in healthy brain were extracted from 12 control subjects belonging to the Unit's normal database. Gray and white matter maps were obtained from the segmented

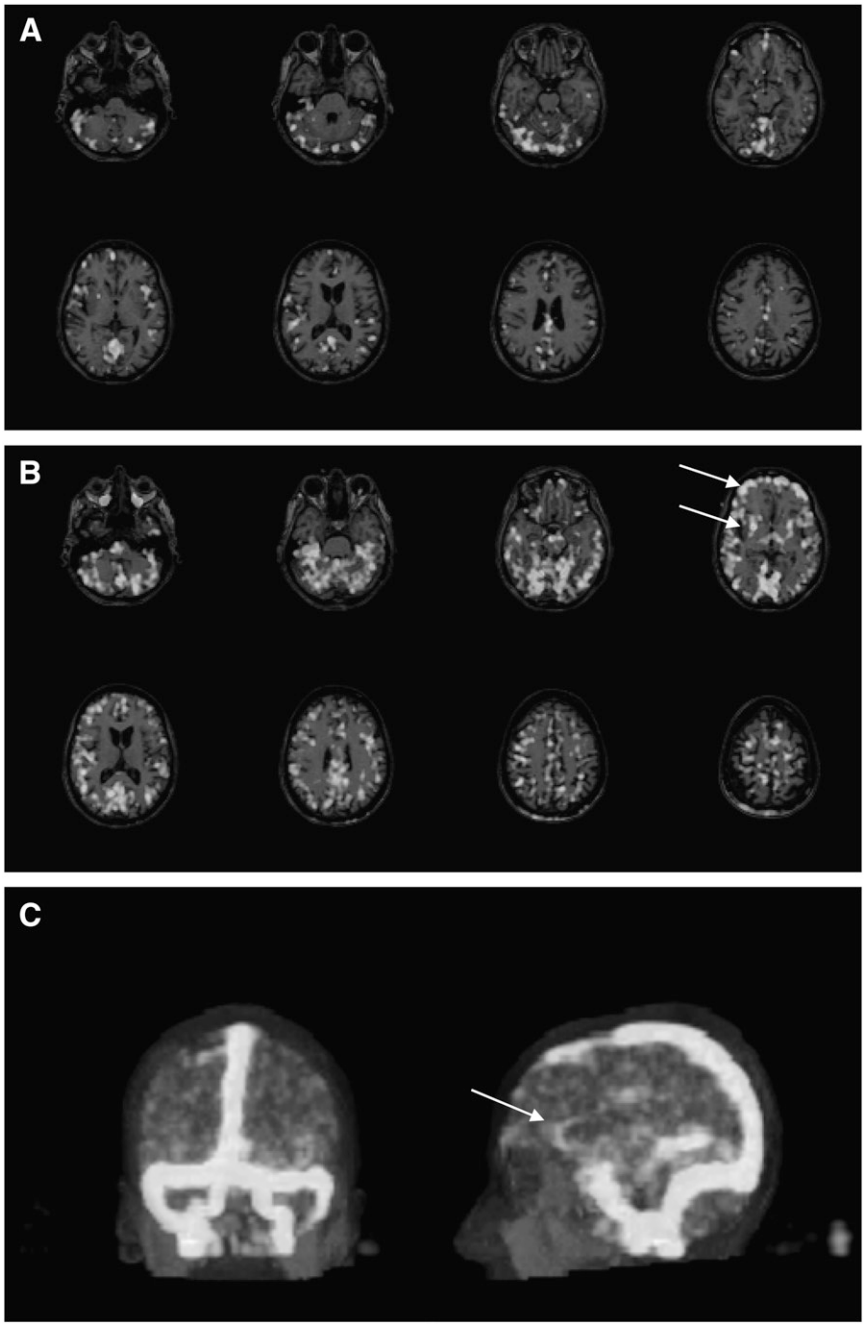

FIGURE 3. HD patient. (A) Map of gray matter reference region extracted by supervised algorithm as overlaid on the coregistered MR image. (B) Map of high PBBS density class. It includes voxels belonging to striatum and frontal cortex (arrows), where microglia activation is expected. (C) Maximum-intensity rendering of blood fraction cluster. Both posterior (left) and lateral (right) views are shown. Note clear detection of venous system but also of major arteries (arrow points to anterior cerebral artery).

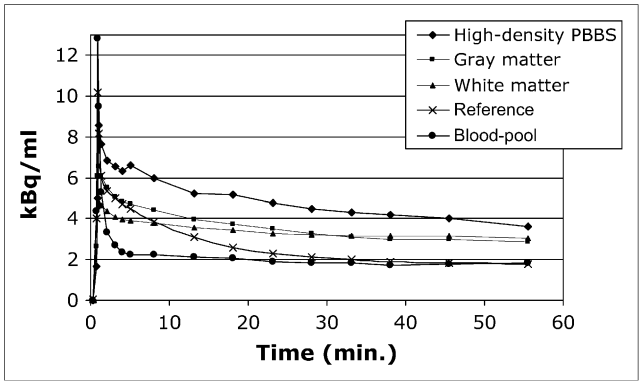

FIGURE 4. Time–activity curves extracted from [^{11}C]-(*R*)-PK11195 dynamic scan of HD patient. ROIs were drawn on areas where high density of PBBS related to microglia activation was expected (caudate, putamen, and globus pallidus), whole gray and white matter. Activity in gray matter reference region and in blood fraction region as extracted by supervised clustering is illustrated. Time–activity curves are decay corrected.

MRI volume and then thresholded (only map values $>$ 90% of maximum value were retained) to minimize the effect of partial volume. These maps were then coregistered to the dynamic scans and multiplied with them to obtain the normalized time courses that were then averaged to obtain the class average normalized time–activity curve.

Definition of Class 3: Pathologic PBBS Binding

To define the kinetic class specific for tissue with intense microglia activation we considered 3 symptomatic patients with HD. All 3 patients had genetically proven disease with an expanded CAG repeat in the IT15 gene on chromosome 4.

Time–activity curves were defined on the striatum and globus pallidus that have well-documented microglia activity in the disease (*16*,*21*) and that were hyperintense on the PET scans (weighted summed average radioactivity images) of these subjects.

Definition of Classes 4, 5, and 6: Blood Pool, Muscle, and Skull

The average time–activity curve specific for the blood fraction was obtained by manually drawing an ROI on the venous sinus of the 12 healthy subjects. Intense signal was identified in muscle and a class kinetic for this tissue was obtained by drawing an ROI on the sternomastoid muscle. A class was also defined for the kinetic of the skull by manually drawing ROIs directly on the PET image.

Validation: Comparison with Blood Input Modeling

The first part of the validation consisted of the comparison between the BP values obtained with blood modeling and those obtained with the reference region extracted by the supervised clustering. Six control subjects were used for whom arterial sampling of the input function was available.

Whole gray and white matter were extracted by segmentation of the MRI volume and then coregistered to the PET. The kinetics of these regions, which have a high signal-to-noise ratio, were inspected using exponential spectral analysis (ESA) (*22*). ESA basis functions spanned the range from 10 s to 60 min. Regions were also manually drawn on the MR image on cerebellum, thalamus, and parietal cortex and the respective time–activity curve extracted from the matched PET volumes.

BP estimates for both sets of regions were calculated using the plasma input function with the formula:

$$BP = \frac{V_{tg} - V_{ref}}{V_{ref}}, \qquad \text{Eq. 5}$$

where V_{tg} and V_{ref} are the volumes of distribution for the target and reference region, respectively, and V_{ref} is used as an estimate of the volume of distribution of the free and nonspecifically bound tracer. The reference region used was the one obtained by the supervised clustering. V_{tg} and V_{ref} were calculated using rank-shaping regularized ESA (RS-ESA) (*23*). RS-ESA is a Bayesian development of ESA that does not rely on the nonnegativity constraints of ESA and produces reliable estimates of volumes of distribution for both plasma and reference modeling. RS-ESA reaches an effective compromise between the reliability of the

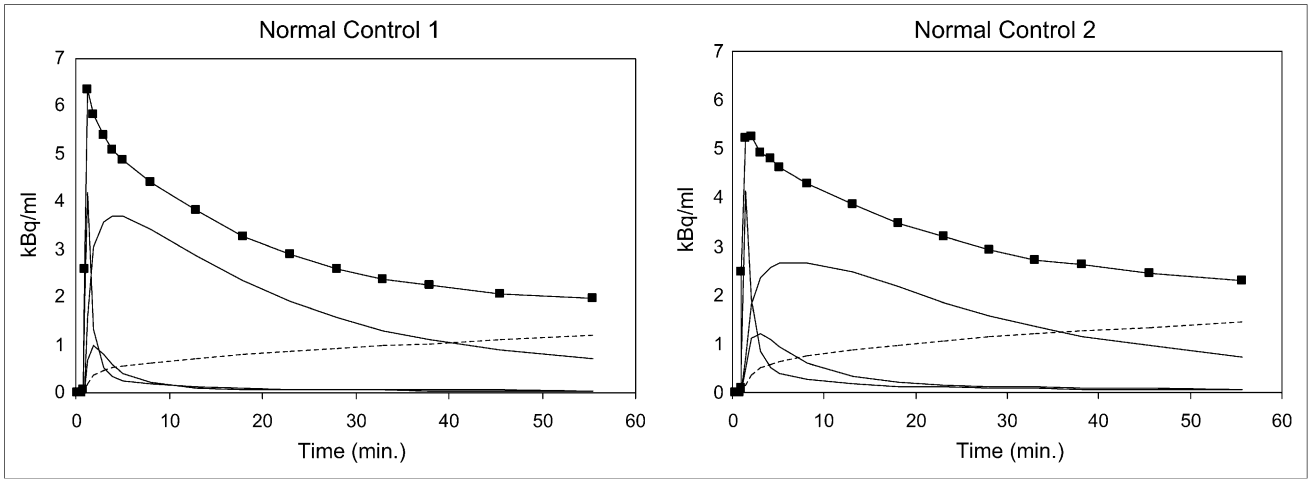

FIGURE 5. Results of application of ESA with blood input function to time–activity curve of whole normal gray matter for 2 healthy control subjects. Time–activity curves are decay corrected. Also shown are ESA fit to data (squares), kinetic components extracted (continuous lines), plus slowly equilibrating component (dashed line) that, by end of scan, accounts for ~75% of total radioactivity.

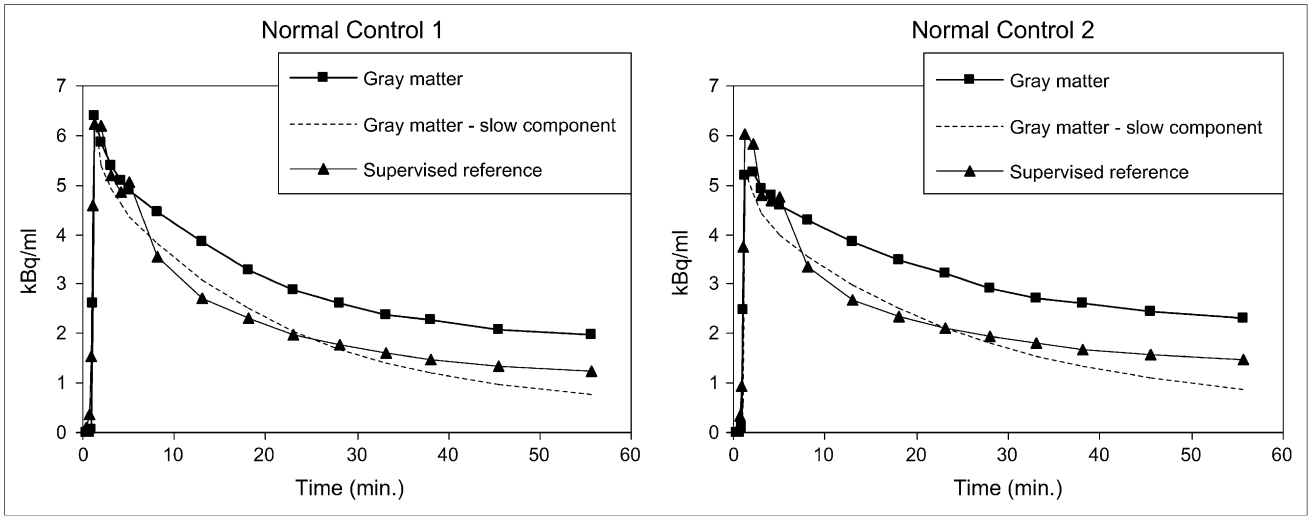

FIGURE 6. For the same subjects as in Figure 7, the slowly equilibrating component of vascular origin was subtracted from the whole gray matter time–activity curve (squares), producing a time–activity curve (dashed line) that was comparable with the time–activity curve of reference region extracted by supervised clustering method (triangles). The ability of the supervised methodology to filter out pixels with significant endothelial binding is illustrated.

estimates obtained by compartmental models with the flexibility of SA that does not require a predefined compartmental structure. BP estimates were also obtained using the reference input by the formula (*24*):

$$BP = V_{tg}^{ref} - 1, \qquad \text{Eq. 6}$$

where V_{tg}^{ref} is the volume of distribution in the target region calculated with RS-ESA using the input extracted by the clustering algorithm. Note that RS-ESA incorporated a blood time–activity curve in the functional base when plasma input was used but obviously this was not possible using a reference tissue input. However, this is not expected to affect the BP estimate significantly. The fraction of signal coming from blood in PK11195 studies is no greater than in any other tracer even at late times because, although the first-pass extraction in brain is low, there is very large uptake of the tracer in peripheral organs (lung, heart, liver, and kidneys).

Finally, BP estimates were calculated using SRTM and the reference region extracted by the supervised algorithm for comparison.

Validation: Test–Retest Reproducibility

The second part of the validation consisted of the assessment of the reproducibility of supervised clustering in comparison with the previous unsupervised approach. We used a set of test–retest data that consisted of 4 subjects with AD scanned twice at an interval of <6 wk. Arterial input data were not available for this cohort. To reproduce a current processing protocol of the Unit, parametric maps were obtained first and ROIs were placed later after normalization into MNI space and application of the latest version of an ROI maximum-probability brain atlas (*25*). The atlas was individualized for each subject by convolving it with the subject's thresholded gray matter map. ROI sampling included hippocampus, amygdala, cerebellum, lateral occipital lobe, anterior and posterior cingulate gyrus, middle frontal gyrus, posterior temporal lobe, parietal cortex, putamen, thalamus (all sampled separately on the left and right), and brain stem.

Parametric maps were produced using both RS-ESA and SRTM. Reproducibility of the 2 clustering methods was assessed by calculating the test–retest variability and the intraclass correlation coefficient (ICC).

RESULTS

Supervised Clustering and Reference Region Extraction

The performance of the supervised clustering is epitomized by the results for one of the 3 HD patients. The supervised algorithm selects as reference region a set of gray matter voxels, mostly in the cerebellum but also in the

TABLE 1
BP Values for 6 Healthy Control Subjects

Region	Plasma modeling (RS-ESA) Mean ± SD	Reference modeling (RS-ESA) Mean ± SD	Reference modeling (SRTM) Mean ± SD
Gray matter	0.26 ± 0.19	0.19 ± 0.14	0.12 ± 0.17
White matter	0.02 ± 0.07	0.07 ± 0.16	0.22 ± 0.17
Cerebellum	0.33 ± 0.26	0.26 ± 0.17	0.20 ± 0.09
Thalamus	0.51 ± 0.52	0.52 ± 0.36	0.27 ± 0.24
Cortex	0.26 ± 0.22	0.22 ± 0.20	0.27 ± 0.24

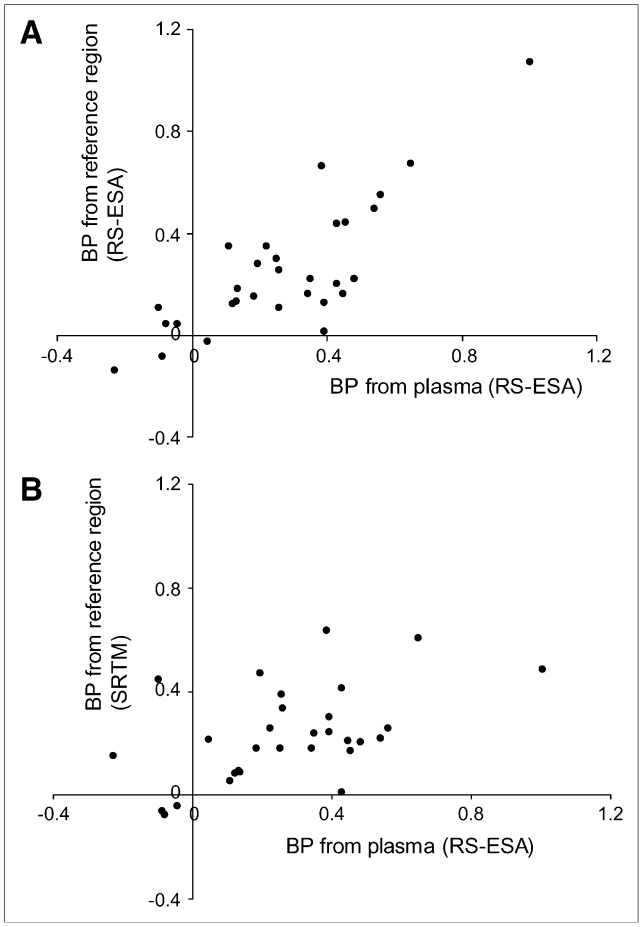

FIGURE 7. Correlation between reference region-derived and plasma-derived BP values. Reference region was extracted by supervised algorithm. BP values with reference region input were calculated using RS-ESA (A) and SRTM (B). In the case of RS-ESA, there was very close agreement and high correlation ($r = 0.811$, $P < 10^{-5}$) between BP values calculated by reference tissue input and those derived from plasma input. SRTM consistently underestimated BP values and correlation with plasma-derived measures was poorer ($r = 0.507$, $P = 0.004$).

cerebral cortex (Fig. 3A). The algorithm clusters into the PBBS-specific binding class regions, where high binding is expected in HD, such as striatum and frontal cortex (Fig. 3B). The algorithm also identifies large areas with significant signal coming from the blood fraction and is able to reconstruct a remarkably clear picture of the blood vessels (Fig. 3C), where sinuses and even the major arteries can be clearly identified.

Figure 4 illustrates, for the same subject as in Figure 3, the time–activity curves of an ROI averaged over putamen, caudate, and globus pallidus, where strong specific signal was expected, the time–activity curves of whole gray matter and whole white matter, and the time–activity curves of the gray matter reference region and blood pool extracted by the supervised clustering. Figure 4 suggests that the time–activity curve of the supervised region is filtered from the contributions of specific binding and white matter but also from signal coming from the blood pool. Indeed, it is noticeable that the kinetic of the blood pool, after the initial fast clearance, levels at a steady, if not slowly, increasing level. This suggests the presence of a slowly equilibrating component in the vasculature and, given the steady clearance of radioactivity (parent tracer and metabolites) measured from arterial blood, it is consistent with binding to the vasculature that can be eminently identified by immunostaining.

These findings were repeated in the other 2 patients with HD. The considerable signal in the blood pool was common to all studies examined, both healthy control subjects and patients.

Comparison Between Reference Input and Plasma Input Modeling

Blood input data were used initially to confirm the presence of a slowly equilibrating kinetic component in brain tissues. Figure 5 shows the kinetic components extracted by ESA on the whole gray matter of healthy volunteers. The result is shown for 2 subjects to illustrate its consistency. Very similar results were obtained in all other control subjects. It is clear from Figure 5 that ESA detects a slowly increasing kinetic component that corresponds to ~75% of the total radioactivity at 60 min. Furthermore, Figure 6 illustrates for the same 2 subjects how—by subtracting from the whole gray matter time–activity curve the slow component extracted by ESA—one obtains a time–activity curve that is comparable with the one of the reference regions obtained by the supervised clustering algorithm. This suggests that the supervised clustering algorithm selects as reference region gray matter voxels that are distant from the vasculature, where the slow kinetic component is prominent. This kinetic component is much slower than the one we apportion to microglia but is very similar to the kinetic of PK11195 previously reported in the heart (*26*). This is consistent with either different transport rates of the tracer or, more likely, different affinities of the PBBS in endothelium and muscle.

This new finding makes the compartmental structure of the kinetic model for [^{11}C]-(*R*)-PK11195 quite complex, as it now requires an additional tissue compartment for the specific binding in the vasculature. This further source of specific binding, plus the expected significant amount of nonspecific binding (*7*), renders the direct estimation of BP values from a compartmental model quite unattractive. However, the ability to extract a valid reference region with no specific binding and the use of RS-ESA, which can calculate robust estimates of the volume of distribution with no prerequisite of assuming a particular compartmental structure, make the task of BP estimation for both plasma and reference region quite straightforward through application of Equations 5 and 6. Using this approach we obtained a very close agreement between the BP estimates obtained with the reference region and the plasma input function as illustrated Table 1. Note the low values of BP

for white matter, clustered around 0 and therefore including negative values, which were expected given the lack of PBBS in normal white matter and the lower vascular density. Mean values for cortical gray matter were 0.26 for plasma-derived BPs, and 0.19 for reference-derived BPs, which are physiologically meaningful given the overall low density of PBBS in the normal brain. Mean values were highest in the thalamus, where increased PBBS density is expected in elderly control subjects (*27*). Note that ESA did not detect a significant endothelial component in the thalamic areas.

Correlation between the reference-derived and plasma input−derived BPs was also high ($r = 0.811$, $P < 10^{-5}$), as illustrated in the scatter plot in Figure 7A.

In this ROI analysis, the simple modeling structure of SRTM lacked the degrees of freedom to describe time–activity curves with high signal-to-noise ratios and the fits were poor. Consequently, there was little correspondence between SRTM-derived BPs and plasma-derived BPs (Table 1), and correlation between the 2 measures was lower ($r = 0.507$, $P < 0.004$; Fig. 7B). In particular, SRTM overestimated BPs in white matter (Table 1), due to the inability of the model to cope with the irreducible spillover of signal from gray matter caused by imperfect segmentation. Note that percentage errors for the estimates of the volumes of distributions were low for both RS-ESA and SRTM (~1.5% for large regions such as cortex and cerebellum, ~3% for thalamus).

Validation: Test–Retest Reproducibility

The final validation consisted of the comparison of the reproducibility of the new reference region extraction with that obtained through the unsupervised algorithm (*13*). Both SRTM and RS-ESA were used to generate parametric maps. RS-ESA performed poorly in the pixel-by-pixel estimation, producing maps with high variability (data not shown). SRTM's simpler structure instead performed well with the high noise levels and the less heterogeneous signal at the pixel level and was selected as the better compromise for the estimation of parametric maps. Therefore, only SRTM results are reported.

Tables 2 and 3 show results for the 4 AD subjects injected with 296 MBq for whom test–retest data were available in terms of mean value, mean of the differences between the first and second scan, percentage mean difference, and the ICC.

Table 2 reports the reproducibility results for SRTM where the reference was extracted with the unsupervised clustering. Care must be taken in the interpretation of this table: Because the reference region selected by the unsupervised algorithm contained specific binding, BP values obtained by SRTM in this case were close to zero if not negative. For those regions with a mean value around 0, the percentage mean difference was therefore abnormally high but is included for completeness. Reproducibility can be better appreciated by looking at the absolute mean differences and at the ICC values.

TABLE 2
Test–Retest BP Values and ICC Obtained Using Reference Region Extracted by Unsupervised Clustering Algorithm

	Unsupervised clustering			
Region	Mean	Mean difference	Percentage difference	ICC
Hippocampus (L)	0.133	0.033	24.54	0.861
Hippocampus (R)	0.155	0.051	32.69	0.909
Amygdala (L)	0.019	0.096	517.53	0.391
Amygdala (R)	0.090	0.057	63.76	0.932
Cerebellum (L)	0.080	0.049	61.49	0.181
Cerebellum (R)	0.093	0.044	47.75	0.660
Brain stem	0.228	0.029	12.76	0.928
Lateral occipital lobe (L)	0.122	0.047	38.09	0.678
Lateral occipital lobe (R)	0.118	0.048	40.35	0.063
Anterior cingulate gyrus (L)	0.156	0.055	35.37	0.667
Anterior cingulate gyrus (R)	0.142	0.045	31.78	0.883
Posterior cingulate gyrus (L)	0.181	0.076	42.18	0.747
Posterior cingulate gyrus (R)	0.191	0.054	28.11	0.903
Middle frontal gyrus (L)	0.099	0.041	41.03	0.081
Middle frontal gyrus (R)	0.088	0.026	29.60	0.726
Posterior temporal lobe (L)	0.130	0.030	23.11	0.425
Posterior temporal lobe (R)	0.134	0.026	19.64	0.399
Parietal cortex (L)	0.133	0.035	26.59	0.817
Parietal cortex (R)	0.117	0.033	28.22	0.813
Putamen (L)	0.191	0.062	32.69	0.844
Putamen (R)	0.148	0.028	19.26	0.536
Thalamus (L)	0.153	0.102	66.22	0.086
Thalamus (R)	0.156	0.120	76.91	0.170
Mean	0.133	0.033	58.25	0.596

TABLE 3
Test–Retest BP Values and ICC Obtained Using Reference Region Extracted by Supervised Clustering Algorithm

Region	Supervised clustering			
	Mean	Mean difference	Percentage difference	ICC
Hippocampus (L)	0.294	0.030	10.20	0.953
Hippocampus (R)	0.280	0.023	8.04	0.782
Amygdala (L)	0.270	0.068	25.00	0.753
Amygdala (R)	0.268	0.020	7.46	0.893
Cerebellum (L)	0.299	0.010	3.34	0.972
Cerebellum (R)	0.292	0.008	2.57	0.987
Brain stem	0.452	0.033	7.19	0.896
Lateral occipital lobe (L)	0.252	0.013	4.96	0.969
Lateral occipital lobe (R)	0.270	0.018	6.48	0.944
Anterior cingulate gyrus (L)	0.261	0.030	11.49	0.971
Anterior cingulate gyrus (R)	0.283	0.043	15.02	0.905
Posterior cingulate gyrus (L)	0.336	0.033	9.67	0.982
Posterior cingulate gyrus (R)	0.312	0.053	16.83	0.93
Middle frontal gyrus (L)	0.237	0.040	16.88	0.848
Middle frontal gyrus (R)	0.228	0.028	12.06	0.84
Posterior temporal lobe (L)	0.264	0.015	5.68	0.964
Posterior temporal lobe (R)	0.251	0.020	7.97	0.929
Parietal cortex (L)	0.228	0.035	15.35	0.794
Parietal cortex (R)	0.226	0.033	14.38	0.743
Putamen (L)	0.395	0.050	12.66	0.891
Putamen (R)	0.399	0.033	8.15	0.928
Thalamus (L)	0.399	0.050	12.53	0.722
Thalamus (R)	0.424	0.043	10.02	0.591
Mean	0.301	0.031	10.61	0.878

Regional ICCs were 0.596, on average, for the BPs obtained using the unsupervised clustering methodology. This value must be compared with the average ICC obtained using the supervised reference extraction—that is, 0.878—as shown in Table 3. In this table, given that BP values are higher, fractional mean differences are more informative and equal to 10.6% on average.

DISCUSSION

One peculiar aspect of [^{11}C]-(*R*)-PK11195 studies in brain is the very scarce presence of the PBBS in the normal brain. This renders the modeling of this tracer particularly difficult because effects of no interest such as tissue heterogeneity and vascular signal become predominant, whereas the abundant presence of the PBBS in the periphery affects the availability of [^{11}C]-(*R*)-PK11195 for binding in the brain. This problem affects the definition of a reference region, a process that already must take into account the unknown location of microglia activation. In this work we have introduced a new supervised clustering procedure, totally automatic, that is able to extract a gray matter reference region devoid of nuisance signal.

A relevant finding of the study is the presence of a slowly equilibrating kinetic component in the tissue time–activity curves. Evidence from immunohistochemistry suggests that this signal is specific for PBBS binding in the vasculature, and its kinetic, although different from that of specific binding to activated microglia, resembles closely the [^{11}C]-(*R*)-PK11195 kinetic in heart (*26*).

The presence of this additional component introduced another level of complexity in the kinetic modeling of ROI time–activity curves. For this task we abandoned compartmental modeling and adopted RS-ESA for the calculation of BP estimates for both plasma input and reference tissue input analyses. The effective extraction of a reference region combined with parameter estimation through RS-ESA provided an excellent agreement between plasma input and reference tissue input−derived BPs that were also highly correlated ($r = 0.811$, $P < 10^{-5}$). This validates further the use of reference region modeling for the quantification of [^{11}C]-(*R*)-PK11195 and allows direct comparison with the plasma input counterpart.

Finally, we investigated the reliability of the new reference extraction when BP parametric maps for [^{11}C]-(*R*)-PK11195 are produced on a test–retest dataset. In this application, given the generally low signal-to-noise ratio in [^{11}C]-(*R*)-PK11195 studies, SRTM was the method of choice for kinetic analysis. Results confirmed a substantial increase in the reliability of the estimates with the new supervised approach (mean ICC = 0.878) compared with the unsupervised approach (mean ICC = 0.596) and low test–retest variability (10.6%).

CONCLUSION

Reference region modeling combined with supervised reference tissue extraction produces reproducible and

reliable parametric maps of [^{11}C]-(*R*)-PK11195 binding in the human brain.

ACKNOWLEDGMENTS

This study was funded in part by the EC-FP6-project DiMI, LSHB-CT-2005-512146A, and by the Parkinson's Disease Society, United Kingdom (MAP 02/04). The authors thank Ralph Myers and Marie Claude Asselin at Hammersmith Imanet for helpful comments and discussion. Hammersmith Imanet provided [^{11}C]-(*R*)-PK11195 and all PET scanning equipment.

REFERENCES

1. Hertz L. Binding characteristics of the receptor and coupling to transport proteins. In: Giessen-Crouse E, ed. *Peripheral Benzodiazepine Receptors*. London, U.K.: Academic Press; 1993:27–51.
2. Gavish M, Bachman I, Shokrun R, et al. Enigma of the peripheral benzodiazepine receptor. *Pharmacol Rev.* 1999;51:629–650.
3. Banati RB. Visualising microglial activation in vivo. *Glia.* 2002;40:206–217.
4. Kreutzberg GW. Microglia: a sensor for pathological events in the CNS. *Trends Neurosci.* 1996;19:312–318.
5. Flugel A, Bradl M, Kreutzberg GW, Graeber MB. Transformation of donor-derived bone marrow precursors into host microglia during autoimmune CNS inflammation and during the retrograde response to axotomy. *J Neurosci Res.* 2001; 66:74–82.
6. Banati RB, Cagnin A, Brooks DJ, et al. Long-term trans-synaptic glial responses in the human thalamus after peripheral nerve injury. *Neuroreport.* 2001;12: 3439–3442.
7. Shah F, Hume SP, Pike VW, Ashworth S, McDermott J. Synthesis of the enantiomers of [N-methyl-^{11}C]PK 11195 and comparison of their behaviours as radioligands for PK binding sites in rats. *Nucl Med Biol.* 1994;21:573–581.
8. Lammertsma AA, Hume SP. Simplified reference tissue model for PET receptor studies. *Neuroimage.* 1996;4:153–158.
9. Kropholler MA, Boellaard R, Schuitemaker A, et al. Development of a tracer kinetic plasma input model for (R)-[^{11}C]PK11195 brain studies. *J Cereb Blood Flow Metab.* 2005;25:842–851.
10. Kropholler MA, Boellaard R, Schuitemaker A, Folkersma H, van Berckel BN, Lammertsma AA. Evaluation of reference tissue models for the analysis of [^{11}C](R)-PK11195 studies. *J Cereb Blood Flow Metab.* 2006;26:1431–1441.
11. Mrak RE, Griffin WS. Glia and their cytokines in progression of neurodegeneration. *Neurobiol Aging.* 2005;26:349–354.
12. Gerhard A, Watts J, Trender-Gerhard I, et al. In vivo imaging of microglial activation with [^{11}C](R)-PK11195 PET in corticobasal degeneration. *Mov Disord.* 2004;19:1221–1226.
13. Gunn RN, Lammertsma AA, Cunningham VJ. Parametric imaging of ligand-receptor interactions using a reference tissue model and cluster analysis. In: Carson R, Daube-Witherspoon M, Herscovitch P, eds. *Quantitative Functional Brain Imaging with Positron Emission Tomography.* San Diego CA: Academic Press; 1998:401–406.
14. Chen J, Gunn S, Nixon M, Myers R, Gunn R. A supervised method for PET reference region extraction. *Proceedings of Medical Image Understanding and Analysis*. London, U.K.; July 2000:179–182.
15. Spinks TJ, Jones T, Bloomfield PM, et al. Physical characteristics of the ECAT EXACT3D positron tomograph. *Phys Med Biol.* 2000;45:2601–2618.
16. Pavese N, Gerhard A, Tai YF, et al. Microglial activation correlates with severity in Huntington disease: a clinical and PET study. *Neurology.* 2006;66:1638–1643.
17. Ranicar AS, Williams CW, Schnorr L, et al. The on-line monitoring of continuously withdrawn arterial blood during PET studies using a single BGO/photomultiplier assembly and non-stick tubing. *Med Prog Technol.* 1991;17:259–264.
18. Luthra S, Osman S, Turton D, Vaja V, Dowsett K, Brady F. An automated system based on solid phase extraction and HPLC for the routine determination in plasma of unchanged [^{11}C]-L-deprenyl; [^{11}C]diprenrophine; [^{11}C]flumazenil; [^{11}C]raclopride; and [^{11}C]Scherring 23390. *J Labelled Comp Radiopharm.* 1993;518–520.
19. Gunn RN, Lammertsma AA, Hume SP, Cunningham VJ. Parametric imaging of ligand-receptor binding in PET using a simplified reference region model. *Neuroimage.* 1997;6:279–287.
20. Lawson C, Hanson R. *Solving Least Squares Problems*. Englewood Cliffs, NJ: Prentice-Hall; 1974:160–165.
21. Sapp E, Kegel KB, Aronin N, et al. Early and progressive accumulation of reactive microglia in the Huntington disease brain. *J Neuropathol Exp Neurol.* 2001;60:161–172.
22. Cunningham VJ, Jones T. Spectral analysis of dynamic PET studies. *J Cereb Blood Flow Metab.* 1993;13:15–23.
23. Turkheimer FE, Hinz R, Gunn RN, Aston JA, Gunn SR, Cunningham VJ. Rank-shaping regularization of exponential spectral analysis for application to functional parametric mapping. *Phys Med Biol.* 2003;48:3819–3841.
24. Gunn RN, Gunn SR, Cunningham VJ. Positron emission tomography compartmental models. *J Cereb Blood Flow Metab.* 2001;21:635–652.
25. Hammers A, Allom R, Koepp MJ, et al. Three-dimensional maximum probability atlas of the human brain, with particular reference to the temporal lobe. *Hum Brain Mapp.* 2003;19:224–247.
26. Charbonneau P, Syrota A, Crouzel C, Valois JM, Prenant C, Crouzel M. Peripheral-type benzodiazepine receptors in the living heart characterized by positron emission tomography. *Circulation.* 1986;73:476–483.
27. Cagnin A, Brooks DJ, Kennedy AM, et al. In-vivo measurement of activated microglia in dementia. *Lancet.* 2001;358:461–467.